

Showcasing research from Shenzhen PURI Materials Technologies Co., LTD., Shenzhen, China.

Phosphorescent [3 + 2 + 1] coordinated Ir(III) cyano complexes for achieving efficient phosphors and their application in OLED devices

This work reports a novel [3 + 2 + 1] coordinated type of neutral iridium complexes, combining the advantages of tridentate bis(NHC) ligands, bidentate cyclometalated ligands ( $C^N$ ) and monodentate cyanide (-CN). Through easy tuning by variation of the bidentate ligands, these iridium complexes display wide range phosphorescent emission, which covers the UV and the visible light range. They display high PLQYs (up to 81%), and good thermal and electrochemical stabilities. In particular, a blue OLED based on **dfppy-CN** exhibits a  $EQE_{max}$  of 22.94% with  $CIE_{x,y}$  of (0.14, 0.24). Furthermore, a small efficiency roll-off of 5.7% was observed at 1000  $cd\ m^{-2}$ .

As featured in:



See Chen Yang, Gang Cheng, Qingdan Yang, Guodan Wei et al., *Chem. Sci.*, 2021, **12**, 10165.

Cite this: *Chem. Sci.*, 2021, **12**, 10165

All publication charges for this article have been paid for by the Royal Society of Chemistry

## Phosphorescent [3 + 2 + 1] coordinated Ir(III) cyano complexes for achieving efficient phosphors and their application in OLED devices†

Yuan Wu,<sup>‡a</sup> Chen Yang, <sup>‡,\*,ab</sup> Jie Liu,<sup>c</sup> Meng Zhang,<sup>d</sup> Weiqiang Liu,<sup>e</sup> Wansi Li,<sup>d</sup> Chengcheng Wu,<sup>a</sup> Gang Cheng, <sup>‡,\*,ef</sup> Qingdan Yang,<sup>\*,b</sup> Guodan Wei <sup>‡,\*,d</sup> and Chi-Ming Che <sup>‡,ef</sup>

A series of neutral [3 + 2 + 1] coordinated iridium complexes bearing tridentate bis-NHC carbene chelates (2,6-bisimidazolylidene benzene), bidentate chelates (C<sup>N</sup> ligands, e.g. derivatives of 2-phenylpyridine), and monodentate ions (halides and pseudo-halides, such as Br, I, OCN and CN ions) have been systematically designed and synthesized. X-ray single crystal structure characterization revealed that the nitrogen atom in C<sup>N</sup> ligands is located *trans* to the carbon atom in the benzene ring in tridentate chelates, while the coordinating carbon atom in C<sup>N</sup> ligands is located *trans* to the monodentate ligands. Photophysical studies reveal that the C<sup>N</sup> ligands play a vital role in tuning the UV absorption and emission properties, while the tridentate bis-NHC carbene chelates influence the lowest absorption band and emission energy when compared to heteroleptic Ir(ppy)<sub>2</sub>(acac) [i.e. molar absorptivities at ~450 nm for ppy-OCN and Ir(ppy)<sub>2</sub>(acac) are 350 M<sup>-1</sup> cm<sup>-1</sup> and 1520 M<sup>-1</sup> cm<sup>-1</sup> and emission maximum peaks are at 465 nm and 515 nm respectively]. Among monodentate ligands that the complexes bear, the group containing the cyanide ligand displays higher emission energy, higher photophysical quantum yields, longer triplet lifetimes and better electrochemical and thermal stabilities than those of cyanate and bromide. Particularly, a blue organic light-emitting diode (OLED) based on dfppy-CN exhibited a maximum external quantum efficiency of 22.94% with CIE coordinates of (0.14, 0.24). Furthermore, a small efficiency roll-off of 5.7% was observed for this device at 1000 cd m<sup>-2</sup>.

Received 11th March 2021  
Accepted 21st June 2021

DOI: 10.1039/d1sc01426a  
[rsc.li/chemical-science](http://rsc.li/chemical-science)

## Introduction

Phosphorescent OLEDs (PhOLEDs), one of the most critical technologies in commercial OLED displays, have many performance advantages over traditional fluorescent OLEDs. For

example, PhOLEDs can reach 100% utilization of its quantum efficiency (QE) whereas that of fluorescent OLEDs can only achieve about 25%.<sup>1–3</sup> Commercial PhOLEDs, especially those employing cyclometalated iridium complexes as emitters, can be commonly found in red, yellow and green colors; achieving efficient deep blue phosphorescent emitters remains a great challenge due to limiting factors such as their poor lifetime (less than one tenth that of blue fluorescent OLEDs<sup>4</sup>) and the great *y* value of Commission International de L'Eclairage (CIE) coordinates. Although many approaches have been applied to improve the efficiency of PhOLEDs, such as developing an appropriate host to balance hole and electron combination to confine subsequent exciton generation and light out-coupling techniques in device construction to improve light efficiency,<sup>5–8</sup> the finding of a satisfactory deep blue emitter is still in great demand. **F1rpic**,<sup>9</sup> a notable phosphorescent blue emitter, was firstly reported to be used to fabricate PhOLED devices, which displayed emission with a peak maximum at 475 nm. However, its CIE coordinates of (0.16, 0.29) showed a sky blue color, instead of pure blue. Subsequently, Chou *et al.* reported a pure-blue PhOLED<sup>10</sup> with CIE coordinates of (0.15, 0.11) and a maximum external quantum efficiency ( $\eta_{ext}$ ) of 11.9% by employing **Ir(fppz)<sub>2</sub>(bdp)** as the emitter, which bears

<sup>a</sup>PURI Materials, 6F, Block A, Jiazhaoye Xindong Kechuang Park, 71st Zone Xindong, Baoan District, Shenzhen, 518133, China. E-mail: [david.yang@purimat.com](mailto:david.yang@purimat.com)

<sup>b</sup>School of Chemical Engineering and Light Industry, Guangdong University of Technology, Guangzhou, 510006, China. E-mail: [qdyang@gdut.edu.cn](mailto:qdyang@gdut.edu.cn)

<sup>c</sup>State Key Laboratory for Mechanical Behavior of Materials, Xi'an Jiaotong University, Xi'an, 710049, China

<sup>d</sup>Tsinghua-Berkeley Shenzhen Institute (TBSI), Tsinghua Shenzhen International Graduate School, Tsinghua University, Shenzhen, 518055, China. E-mail: [weiguodan@sz.tsinghua.edu.cn](mailto:weiguodan@sz.tsinghua.edu.cn)

<sup>e</sup>State Key Laboratory of Synthetic Chemistry, HKU-CAS Joint Laboratory on New Materials, Department of Chemistry, The University of Hong Kong, Pokfulam Road, Hong Kong SAR, China. E-mail: [gcheng@hku.hk](mailto:gcheng@hku.hk)

<sup>f</sup>HKU Shenzhen Institute of Research and Innovation, Shenzhen 518053, China

† Electronic supplementary information (ESI) available: Details of X-ray crystallographic data, photophysical, electrochemical, and thermal properties, DFT calculations, and device fabrication and synthesis of these complexes are provided. CCDC 2068837–2068839. For ESI and crystallographic data in CIF or other electronic format see DOI: 10.1039/d1sc01426a

‡ Y. W. and C. Y. contributed equally to this work.



a nonconjugated, high ligand-field strength benzyl phosphine chelate ligand. In 2016, Forrest and Thompson reported a stable deep-blue phosphorescent iridium complex *fac*-Ir(**pmp**)<sub>3</sub> for achieving the most deep-blue PhOLED<sup>11</sup> device so far with a  $\eta_{\text{ext}}$  of 10.1% and CIE coordinates of (0.16, 0.09), which meets the requirements of the National Television System Committee (NTSC) for stringent blue. Currently, the most efficient deep blue PhOLED<sup>12</sup> with a  $\eta_{\text{ext}}$  of 31.9% and CIE coordinates of (0.14, 0.19) had been fabricated by employing deep-blue phosphorescent (**dfpysipy**)<sub>2</sub>Ir(**mic**).

Most of the neutral iridium complexes for the fabrication of PhOLEDs are with a configuration of one iridium metal center, and three homoleptic/heteroleptic bidentate ligands, noted as [2 + 2 + 2] coordinated type. The classic [2 + 2 + 2] phosphors in the application of PhOLEDs are **FIripic**,<sup>9,13–15</sup> *fac*-Ir(**ppy**)<sub>3</sub> (ref. 16 and 17) and **Ir(piq)**<sub>2</sub>(**acac**).<sup>18</sup> Additionally, a configuration of one iridium metal center and two heteroleptic tridentate chelates for a series of neutral [3 + 3] coordinated iridium complexes had been reported by Chi *et al.*<sup>19–23</sup> These [3 + 3] iridium complexes have shown their advantages in rigidity and durability in application. An isoquinolinyl-functionalized red emitter (**pz<sup>Ph</sup>py<sup>B</sup>ph<sup>B</sup>**)Ir(**pziqph**),<sup>20</sup> with a unity PLQY, had been fabricated as a red PhOLED, giving a max.  $\eta_{\text{ext}}$  of 28.17% and CIE coordinates of (0.63, 0.37). Subsequently, a carbazolyl-functionalized emitter **Cz-5**,<sup>23</sup> with a high photoluminescent quantum yield (PLQY  $\sim$  96.2%), had been fabricated as a blue PhOLED, displaying a good performance with a max.  $\eta_{\text{ext}}$  of 18.7% and CIE coordinates of (0.145, 0.218). To date, neutral iridium complexes with a configuration of [3 + 2 + 1] coordination have been reported to commonly have monoanionic N<sup>+</sup>C<sup>+</sup>N or C<sup>+</sup>N<sup>+</sup>N pincer chelates, where N stands for nitrogen atoms in pyridinyl,<sup>24–27</sup> benzimidazoyl,<sup>28,29</sup> pyrazolyl,<sup>30</sup> and benzothiazolyl or benzoxazolyl<sup>31</sup> ligands. However, a few of these complexes in form of  $[(\text{N}^+\text{C}^+\text{N})\text{Ir}(\text{C}^+\text{N})\text{Cl}]$  which have been fabricated as PhOLEDs<sup>25</sup> face problems, such as the degradation of halide ligands from Ir atoms,<sup>30</sup> and the emission origin competition between tridentate and bidentate chelates<sup>25</sup> in the complexes. On the other hand, most of these complexes show emission covering from the green to red region, and still suffered from blue chromaticity.

Herein, to address these shortcomings, intrinsic ligand design and adjustments should be considered for fulfilling the criterion of new emitters. For example, significant endeavors have been made to achieve stable high quantum efficiency blue phosphors from archetypal green emitters, *fac*-Ir(**ppy**)<sub>3</sub>,<sup>32</sup> using strategies such as: (i) stabilizing the highest occupied molecular orbital (HOMO) by the addition of electron-withdrawing groups on the phenyl rings,<sup>33</sup> (ii) destabilizing the lowest unoccupied molecular orbital (LUMO) by the replacement of azolyl rings with the pyridyl ring. Principally, the energy difference between an excited triplet state and a metal-centered (<sup>3</sup>MC) dd state would determine the quantum efficiency (QE) of an emitter. However, for a triplet blue emitter, the energy difference for the above states is quite small; the triplet metal-centered (<sup>3</sup>MC) dd state can be populated at ambient temperature, leading to geometrical distortion, even a bond dissociation and/or the degradation of an excited molecule.<sup>34</sup> To avoid the population of <sup>3</sup>MC dd

states, some strategies have been implemented, such as using strong-field ligands to create strong metal-ligand bonds,<sup>35</sup> increasing rigidity of the coordinated ligand to prevent distortions in the excited state.<sup>22,36</sup>

N-Heterocyclic carbenes (NHC),<sup>35–42</sup> featuring strong  $\sigma$ -donating and weak  $\pi$ -accepting properties,<sup>43</sup> are regarded as an excellent candidate to destabilize the empty  $d_{\sigma}$  orbital (major participation in the <sup>3</sup>MC state) as well as to stabilize the filled  $d_{\pi}$  orbital (an important role in the emissive state, especially for the <sup>3</sup>MLCT state), thus alleviating the promotion of an electron into the <sup>3</sup>MC dd state. The utilization of ligands containing NHC ligands in transition metal complexes had been documented and regarded as an effective strategy to enhance the phosphorescence of triplet emitters.<sup>44</sup> However, [3 + 2 + 1] iridium complexes containing tridentate ligands which bear bis(NHC) ligands are yet to be investigated. Wong *et al.* reported a class of [3 + 2 + 1] iridium complexes<sup>45</sup> containing tridentate bis(NHC) ligands, wherein bipyridine served as the bidentate ligand and hydride as the monodentate ligand. As a result, these complexes are inherently salts, leading a hurdle in utilization through evaporated process into fabrication as PhOLEDs. Similar to the NHC carbene ligand, a cyanide ion,<sup>46</sup> featuring strong  $\sigma$ -donating and unoccupied weak  $\pi$ -accepting orbitals, could promote the energy level of <sup>3</sup>MC states and accept the electron pair in the filled  $d_{\pi}$  orbital from the metal. In contrast, the cyanide ion offers a negative charge, which shows affinity toward the positive iridium metal center, thus leading to a more stable bond. However, there is still a shortage of its application in current literature studies<sup>47,48</sup> with the purpose of tuning the emission color in Ir(**III**) cyano complexes.

To date, bidentate cyclometalated ligands, 2-phenylpyridine as the prototypal structure, have played an extraordinary important role in tuning the emission colors in phosphorescent iridium complexes. With an aim to build a novel type of neutral iridium complex, a series of [3 + 2 + 1] coordinated iridium complexes had been designed and developed herein by using the strategy of combining the advantages of tridentate bis(NHC) ligands and bidentate cyclometalated ligands. This class of emitters display emission covering the whole visible light region, including blue, yellow, orange, and red emitters with the CIE coordinates ranging from 0.1 to 0.6. And most of these blue emitters display quantum yields greater than 50% and summary of CIE<sub>x,y</sub> below 0.3, which satisfied our criteria as good blue emitters.

## Results and discussion

### Synthesis

The synthetic route for the [3 + 2 + 1] coordinated iridium complexes are depicted in Chart 1. [3 + 2 + 1] coordinated Ir(**III**) halide complexes were synthesized from a two-step reaction. The first step was to combine the tridentate C<sup>+</sup>C<sup>+</sup>C ligand and an iridium precursor  $[\text{Ir}(\text{u-Cl})(\text{COD})]_2$  (COD = 1,5-cyclooctadiene) in the presence of triethylamine (NEt<sub>3</sub>) in acetonitrile (CH<sub>3</sub>CN) solution and the mixture was refluxed under a nitrogen atmosphere at 90 °C for 8 hours. After that, the volatiles were removed under vacuum leaving an orange



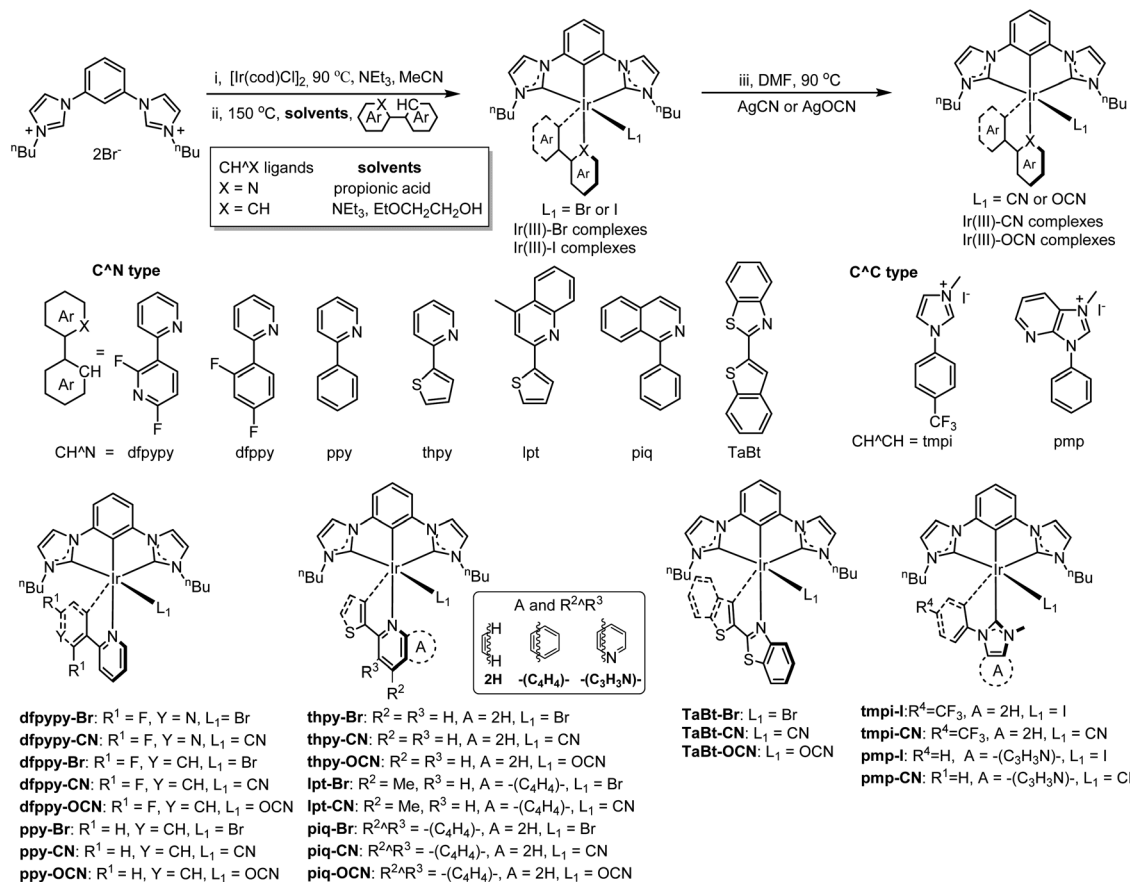


**Chart 1** Synthesis of [3 + 2 + 1] iridium complexes. [Reagents and conditions: (i)  $[\text{Ir}(\text{cod})\text{Cl}]_2$  (0.5 eq.),  $\text{NEt}_3$  0.5–1 mL, MeCN 10 mL, 90 °C; (ii)  $\text{CH}^{\text{A}}\text{X}$  ligands (1 eq.), solvents (X = N, propionic acid; X = CH, 2-ethoxyethanol, triethylamine as the base), 150 °C. (iii) 1,  $\text{AgCN}$  or  $\text{AgOCN}$  (2 eq., Celite), DMF, 2 h,  $\text{N}_2$  atmosphere for all steps], and structures of complexes.

residue. The next step, without further isolation, the residue was treated with the bidentate C≡N or C≡C ligands in propionic acid or EtOCH<sub>2</sub>CH<sub>2</sub>OH solution at 150 °C (N<sub>2</sub> atmosphere) to give the Ir(III)-Br or the Ir(III)-I complexes. The Ir(III)-CN or Ir(III)-OCN complexes were obtained by metathesizing the Ir(III)-Br or Ir(III)-I complexes with AgCN or AgOCN in DMF at 90 °C, respectively. The desired Ir(III) complexes were purified by column chromatography and characterized by nuclear magnetic resonance (NMR) and mass spectrometry.

## Crystallography

The crystal of **thpy-Br** was grown by steadily cooling down the hot dimethyl sulfoxide solution of the complex to room temperature; the crystal of **TaBt-CN** was grown by slow evaporation of dichloromethane ( $\text{CH}_2\text{Cl}_2$ ) solution of the complex into hexane and the crystal of **dfppy-OCN** was grown by slow diffusion of diethyl ether into acetonitrile solution of the complex. The molecular structures of these complexes were examined by single-crystal X-ray crystallography.

The structures are depicted in Fig. 1, and the crystallographic data, selected bond distances and angles are summarized in Table S1 and S2, respectively, see the ESI.† They all adopt a distorted octahedral coordination geometry around the

iridium atom with one tridentate  $\text{C}^{\text{C}}\text{C}^{\text{C}}$  ligand, one bidentate  $\text{C}^{\text{N}}\text{N}$  ligand and a monodentate ligand ( $-\text{Br}$ ,  $-\text{CN}$  or  $-\text{OCN}$ ). The  $\text{C}_{\text{NHC}}\text{--Ir}$  bond distances and the related  $\text{C}_{\text{NHC}}\text{--Ir--C}_{\text{NHC}}$  bite angles of **thpy-Br**, **TaBt-CN**, **dfppy-OCN** are in the range of 2.04–2.06 Å and 154.8–156.0° respectively, in consistent with those observed in Ir(III) complexes featuring similar pincer chelates. The N atom in the  $\text{C}^{\text{N}}\text{N}$  ligand is located at the *trans* position of the  $\text{C}_{\text{Ph}}$  atom of the  $\text{C}^{\text{C}}\text{C}^{\text{C}}$  ligand with a  $\text{N--Ir--C}$  angle of 173.7(3)° (**thpy-Br**), 172.07(19)° (**TaBt-CN**) and 173.07(18)° (**dfppy-OCN**), respectively. The  $\text{N--Ir--C}$  angles in the five-

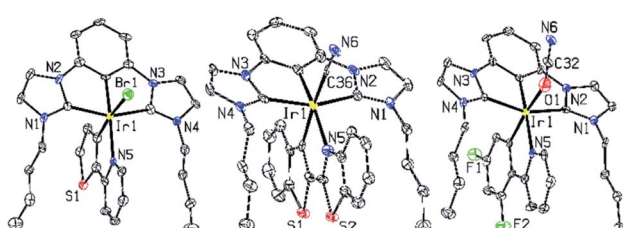


**Fig. 1** ORTEP diagram of thpy-Br, TaBt-CN and dfppy-OCN showing the labeling scheme of the atoms. Ellipsoids are at the 50% probability level, and hydrogen atoms and solvent molecules were omitted for clarity.

membered chelated ring based on the C<sup>N</sup> ligand are 77.95(19) $^\circ$ , 78.87(18) $^\circ$  and 77.95(19) $^\circ$  in **thpy-Br**, **TaBt-CN** and **dfppy-OCN**, respectively. The bond length of Ir-Br is 2.6029(9)  $\text{\AA}$  for **thpy-Br** and those of Ir-C<sub>CN</sub> and Ir-O<sub>OCN</sub> are 2.024(6)  $\text{\AA}$  for **TaBt-CN** and 2.143(5)  $\text{\AA}$  for **dfppy-OCN** respectively.

### Photophysical studies

Absorption and phosphorescent emission spectra of all the Ir(III) complexes were recorded in degassed  $\text{CH}_2\text{Cl}_2$  solution and a thin polymethylmethacrylate (PMMA) polymer film (2 wt% of Ir(III) complexes) at ambient temperature, and are shown in Fig. 2 and S1, S2 (ESI $^\ddagger$ ). The photophysical data are tabulated in Table 1 and phosphorescent solid-state emission spectra at ambient temperature and low temperature (77 K) are shown in Fig. S3–S5 (ESI $^\ddagger$ ). As expected, the high-energy absorption bands below 330 nm ( $\epsilon > 1 \times 10^4 \text{ M}^{-1} \text{ cm}^{-1}$ ) were assigned to the ligand-centered ( $\pi\pi^*$ ) transitions. The moderately intense absorption at a longer wavelength of 330–400 nm ( $3 \times 10^3 < \epsilon < 1 \times 10^4 \text{ M}^{-1} \text{ cm}^{-1}$ ) is assigned to a mixed transition that contains both spin-allowed singlet metal-to-ligand charge transfer ( $^1\text{MLCT}$ ) and singlet ligand-centered/ligand-to-ligand charge transfer ( $^1\text{LC}/^1\text{LLCT}$ ) transitions. As shown in Fig. 1a, the absorption bands for **ppy-Br**, **ppy-OCN** and **ppy-CN** (ppy group) beyond 400 nm ( $\epsilon < 2 \times 10^3 \text{ M}^{-1} \text{ cm}^{-1}$ ) display very different characteristics from those of **(ppy)<sub>2</sub>Ir(acac)**, indicating weak triplet metal-to-ligand charge transfer ( $^3\text{MLCT}$ ) transitions in

these absorption bands for this group. On the other hand, the cyanide ligand in **ppy-CN** leads to more hypsochromic shift in the ppy group of Ir(III) complexes, resulting in a very weak  $^3\text{MLCT}$  characteristic absorption tail beyond 450 nm. This trend for the lowest absorption bands [ $\lambda(\text{CN}) < \lambda(\text{Br}) \sim \lambda(\text{OCN})$ ] is commonly found in all the groups of Ir(III) complexes installing the same C<sup>N</sup> ligands. Further modification by using difluorinated ppy ligands (dfppy and dfpypy ligands) and C<sup>C</sup> type ligands (tmpi and pmp ligands) leads to hypsochromic shifts with the lowest absorption band order of  $\lambda(\text{tmpi}) < \lambda(\text{pmp}) < \lambda(\text{dfpypy}) < \lambda(\text{dfppy})$  in Fig. 1b. Bathochromic shifts [ $\lambda(\text{thpy}) < \lambda(\text{lpt}) < \lambda(\text{piq}) < \lambda(\text{TaBt})$ ] are found for the lowest absorption bands for those C<sup>N</sup> ligands with extending  $\pi$ -conjugations, assigned to the mixing of spin-forbidden  $^3\text{MLCT}$  and  $^3\text{LC}/^3\text{LLCT}$  transitions.

All the Ir(III) complexes feature structured emission profiles with peaks at 386–609 nm in a degassed  $\text{CH}_2\text{Cl}_2$  solution (Fig. 2d–f and S1 and S2 in the ESI $^\ddagger$ ). It is interesting to note that the emission color can be easily tuned from the UV to red region through the substitution of different bidentate ligands. All the Ir(III) complexes exhibit the luminescent characteristics of their bidentate ligands including cyclometalated C<sup>N</sup> and NHC C<sup>C</sup> types. As shown in Fig. 2d, the ppy group of iridium complexes displays distinct structured emission profiles while **(ppy)<sub>2</sub>Ir(acac)** shows a structureless emission band which originated from  $^3\text{MLCT}$  transitions, indicating that the emission for the

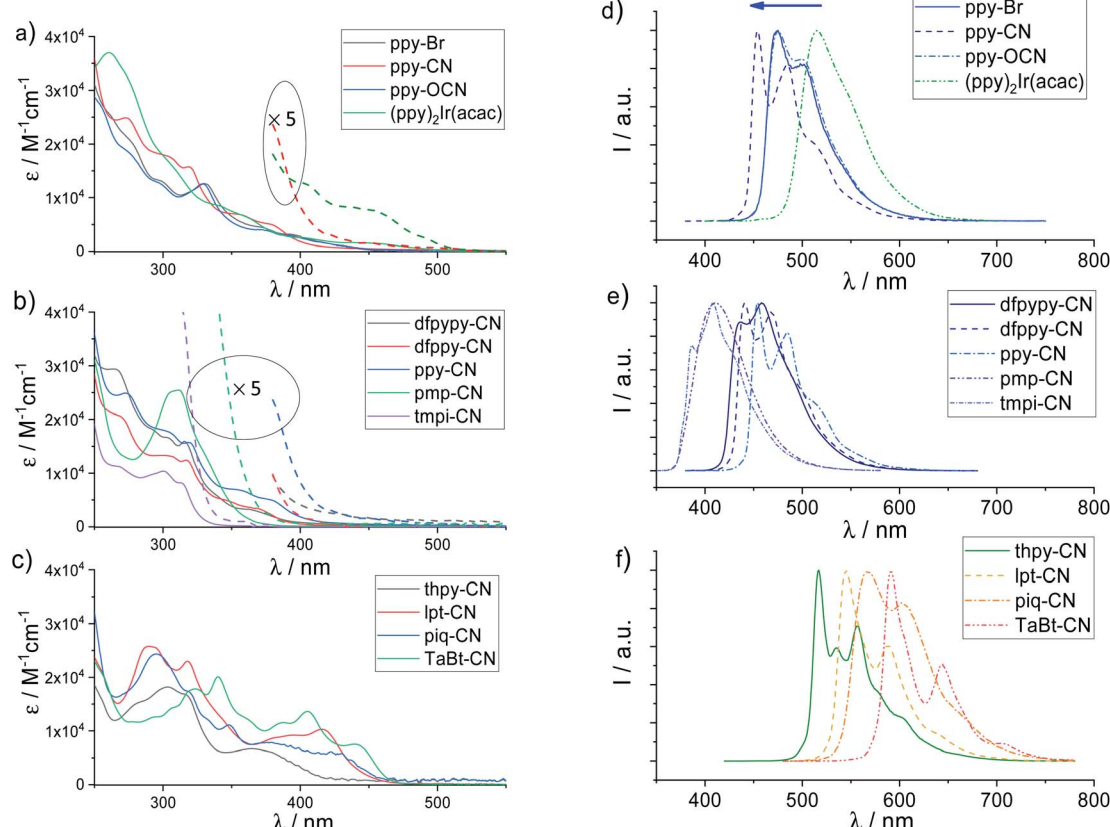


Fig. 2 (a–c) UV-vis molar absorptivity and (d–f) emission of iridium complexes in  $\text{CH}_2\text{Cl}_2$  (conc.:  $\sim 2.0 \times 10^{-5} \text{ M}$ ).



Table 1 Photophysical data for [3 + 2 + 1] iridium complexes

	UV-Vis absorption		Emission		Film <sup>b</sup>	Color <sup>a</sup>	
	Fluid <sup>a</sup>		Fluid <sup>a</sup>				
	$\lambda_{\text{max}}/\text{nm} (\varepsilon \times 10^3/\text{M}^{-1} \text{ cm}^{-1})$	$\lambda_{\text{max}}/\text{nm} (\Phi; \tau/\mu\text{s})$	CIE <sub>(x, y)</sub>	$\lambda_{\text{max}}/\text{nm} (\Phi; \tau/\mu\text{s})$	CIE <sub>(x, y)</sub>		
<b>tmpi-I</b>	250 (24.95), 300 (10.65)		397, 418 (N.A. <sup>c</sup> ; 0.91)	(0.157, 0.052)	397, 418 (N.D. <sup>c</sup> ; 4.72)	(0.195, 0.184)	
<b>tmpi-CN</b>	270 (11.5), 300 (10.9), 315 (8.4), 350 (0.69)		386, 408 (0.14; 1.73)	(0.157, 0.039)	385, 407 (0.56; 7.6)	(0.157, 0.044)	
<b>pmp-I</b>	250 (25.85), 313 (20.5), 359 (4.0)		444 (0.10; 0.72)	(0.154, 0.116)	420 (0.06; 0.90)	(0.158, 0.070)	
<b>pmp-CN</b>	311 (26.1), 331 (13.8), 359 (2.66)		410 (0.20; 0.87)	(0.157, 0.037)	398 (0.56; 3.85)	(0.160, 0.049)	
<b>dfppy-Br</b>	271.67 (15.6), 322.55 (9.35), 384.15 (1.25)		480 (0.12; 0.34)	(0.176, 0.313)	480 (0.69; 2.36)	(0.167, 0.288)	
<b>dfppy-CN</b>	265 (29.4), 292 (18.2), 304 (16.6), 316 (15.9), 339 (5.84), 363 (3.24), 423 (0.51)		436 (0.81; 5.76), 458	(0.146, 0.114)	436, 456 (0.78; 4.89)	(0.149, 0.109)	
<b>dfppy-Br</b>	273 (21.0), 296 (12.9), 326 (12.8), 361 (4.4), 384 (2.95), 444 (0.35)		463 (0.015; 0.16), 480	(0.144, 0.217)	462 (0.55; 1.47), 481	(0.145, 0.252)	
<b>dfppy-CN</b>	269 (20.4), 297 (13.2), 317 (12.3), 344 (4.97), 368 (3.37), 409 (0.29)		441 (0.67; 4.86), 468	(0.144, 0.138)	440 (0.86; 4.51), 466	(0.145, 0.127)	
<b>dfppy-OCN</b>	271 (19.0), 292 (13.0), 326 (12.8), 363 (3.52), 388 (2.22), 444 (0.3)		465 (0.58; 1.78), 481	(0.141, 0.244)	463 (0.80; 1.74), 482	(0.142, 0.230)	
<b>ppy-Br</b>	274 (21.2), 298 (13.1), 330 (12.6), 372 (4.5); 393 (3.19), 450 (0.25)		473 (0.045; 0.22), 502	(0.152, 0.286)	474 (0.69; 1.9), 501	(0.156, 0.379)	
<b>ppy-CN</b>	273 (24.8), 304 (17.6), 318 (15.6), 356 (6.75), 377 (5.04); 423 (0.69)		454 (0.74; 6.55), 485, 511	(0.145, 0.225)	453 (0.77; 5.30), 484, 515	(0.145, 0.212)	
<b>ppy-OCN</b>	274 (18.7), 297 (12.7), 329 (12.6), 372 (4.02), 394 (2.93), 463 (0.35)		475 (0.58; 1.79), 499	(0.153, 0.384)	475 (0.91; 1.65), 501	(0.151, 0.368)	
<b>Irpic</b>	284 (27.0), 318 (14.2), 340 (7.89), 380 (5.54), 416 (2.89), 456 (0.56)		466 (0.69; 1.82), 493	(0.144, 0.286)	466 (0.88; 1.67),	(0.141, 0.277)	
<b>(ppy)<sub>2</sub>Ir(acac)</b>	260 (37.0), 305 (16.4), 342 (8.39), 364 (5.99), 405 (2.49), 454 (1.52), 493 (0.46)		515 (N.D. <sup>c</sup> ; 0.73)	(0.325, 0.622)	516 (N.D. <sup>c</sup> ; 1.96)	(0.312, 0.624)	
<b>thpy-Br</b>	277 (13.0), 306 (17.9), 327 (15.3), 374 (5.61), 399 (4.3), 527 (0.69; 16.4), 546, 421 (3.03), 455 (0.19)		528 (0.69; 11.9), 547, 569, 617	(0.383, 0.600)	528 (0.69; 11.9), 547, 570, 617	(0.382, 0.597)	
<b>thpy-CN</b>	284 (14.8), 303 (17.5), 316 (16.1), 364 (6.0), 379 (5.3), 517 (0.6; 34.3), 535, 556, 429 (0.32)		556, 600	(0.353, 0.614)	516 (0.60; 29.0), 534, 556, 602	(0.352, 0.611)	
<b>thpy-OCN</b>	310 (21.1), 326 (19.1), 374 (6.5), 400 (4.6), 421 (3.45), 528 (0.54; 16.1), 547, 455 (0.48)		569, 594, 618	(0.384, 0.599)	528 (0.63; 13.7), 546, 569, 617	(0.377, 0.589)	
<b>lpt-Br</b>	288 (25.1), 331 (21.9), 399 (7.27), 434 (7.88), 474 (2.18)	558 (0.75; 6.67), 601, 657	(0.493, 0.504)	560 (0.77; 5.64), 603, 658	(0.496, 0.501)		
<b>lpt-CN</b>	291 (25.7), 318 (23.0), 392 (9.17), 416 (10.3), 474 (0.32)	545 (0.78; 16.0), 588, 638	(0.449, 0.546)	547 (0.71; 13.2), 591, 642	(0.443, 0.550)		
<b>piq-Br</b>	297 (22.7), 332 (18.2), 329 (18.5), 348 (12.8), 378 (7.2), 581 (0.60; 4.46), 452 (3.62), 532 (0.40)	617	(0.571, 0.428)	581 (0.65; 3.3), 618	(0.561, 0.434)		
<b>piq-CN</b>	295 (23.5), 318 (16.5), 332 (11.4), 348 (10.3), 379 (7.0), 568 (0.49; 11.2), 431 (4.9), 532 (0.40)	602	(0.534, 0.464)	563 (0.58; 8.95), 600	(0.523, 0.475)		
<b>piq-OCN</b>	295 (22.7), 318 (18.2), 329 (18.5), 348 (12.8), 379 (7.2), 580 (0.62; 3.9), 614, 450 (3.66), 505 (0.47)	671	(0.566, 0.433)	582 (0.66; 2.93), 617	(0.567, 0.432)		
<b>TaBt-Br</b>	308 (15.0), 328 (19.4), 343 (20.4), 368 (7.8), 398 (7.5), 607 (0.27; 7.42), 663, 416 (8.8), 468 (5.53)	663, 730	(0.660, 0.340)	607 (0.31; 6.08), 663, 728	(0.657, 0.343)		
<b>TaBt-CN</b>	308 (14.4), 324 (17.8), 340 (20.1), 360 (12.4), 387 (11.5), 406 (13.6), 440 (7.5)	644, 706	(0.617, 0.382)	591 (0.37; 12.6), 644, 705	(0.615, 0.384)		
<b>TaBt-OCN</b>	328 (31.0), 343 (30.8), 371 (10.6), 400 (10.6), 418 (13.1), 447 (7.84), 468 (8.53)	665, 730	(0.661, 0.339)	607 (0.34; 6.17), 664, 727	(0.655, 0.345)		

<sup>a</sup> Data were recorded in a degassed  $\text{CH}_2\text{Cl}_2$  solution (concentration of  $\sim 2 \times 10^{-5} \text{ M}$ ). <sup>b</sup> Data were recorded in thin-films (2 wt% in PMMA) at room temperature. <sup>c</sup> N.A. and N. D. stand for not available and not detected.



ppy group majorly comes from  $^3\text{LC}/^3\text{LLCT}$  transitions. Additionally, significant hypsochromic shifts as well as greater structured-profiles are observed for the emission peaks of **ppy**-CN compared to those of **ppy**-Br and **ppy**-OCN, revealing greater  $^3\text{LC}/^3\text{LLCT}$  characteristics in the triplet excited states in line with the less  $^3\text{MLCT}$  transitions for **ppy**-CN from the observations in their UV-vis absorption spectra.

The emission spectra of Ir(III) cyano (Ir(III)-CN) complexes are depicted in Fig. 2e and f. Because the strong ligand field of NHC could widen the energy gap by elevating the LUMO levels, **tmpi**-CN and **pmp**-CN complexes display ultraviolet and deep-blue emission ( $\lambda = 386$  and  $410$  nm, Fig. 2e). For those Ir(III)-CN complexes with functionalized C<sup>N</sup>N ligands, benefiting from electron-withdrawing fluorine groups on the C-chelating block which lower its HOMO level, the emission peak is blue-shifted from  $454$  nm of **ppy**-CN to  $440$  nm of **dfppy**-CN. Further replacing the phenyl ring with a fluorinated pyridine ring results in a more hypsochromic shift of the maximum emission for **dfppy**-CN ( $436$  nm). Upon the substitution of pyridine with isoquinoline that possesses a more extended conjugation, **piq**-CN ( $568$  nm) shows a significant bathochromic emission relative to **ppy**-CN. The complexes **thpy**-CN ( $517$  nm), and **lpt**-CN ( $545$  nm) bearing an electron-donating thiophene group as the C-chelating block also show red-shift emission relative to **ppy**-CN. For the C<sup>N</sup>N ligands with a benzothiazole ligand as the N-chelating block and benzothiophene ligand as the C-chelating block, complex **TaBt**-CN exhibits the lowest red emission at  $591$  nm.

The influence of variation of the monodentate ligand (–Br, –OCN or –CN) of Ir(III) complexes composed of the same tridentate and bidentate ligands had also been investigated. The emission spectra of Ir(III)-Br and Ir(III)-OCN complexes are superimposed, while Ir(III)-CN complexes exhibit a *ca.*  $10$ – $30$  nm blue-shift. Such significant influence of the cyanide ligand can be rationalized by its strong electron-withdrawing effect, which leads to the lowering of the HOMO energy and results in a blue-shifted emission.

It is worth noting that all the Ir(III)-CN complexes exhibit a blue-shift as compared to the corresponding well-known [2 + 2 + 2] coordinated homo/heteroleptic Ir(III) complexes bearing the same bidentate ligands: **tmpi**-CN ( $386$  nm,  $\Phi = 0.56$ ) *vs.* **mer-Ir(tmpi)<sub>3</sub>** ( $412$  nm,  $\Phi = 0.72$ ),<sup>49</sup> **pmp**-CN ( $410$  nm,  $\Phi = 0.56$ ) *vs.* **fac-Ir(pmp)<sub>3</sub>** ( $418$  nm,  $\Phi = 0.76$ ),<sup>11</sup> **dfppy**-CN ( $436$  nm,  $\Phi = 0.81$ ) *vs.* **fac-Ir(dfppy)<sub>3</sub>** ( $438$  nm,  $\Phi = 0.43$ ),<sup>50</sup> **ppy**-CN ( $454$  nm,  $\Phi = 0.74$ ) *vs.* **fac-Ir(ppy)<sub>3</sub>** ( $514$  nm,  $\Phi = 0.40$ ),<sup>51</sup> **dfppy**-CN ( $441$  nm,  $\Phi = 0.67$ ) *vs.* **fac-Ir(dfppy)<sub>3</sub>** ( $468$  nm,  $\Phi = 0.43$ ),<sup>51</sup> and **Flrpic** ( $469$  nm,  $\Phi = 0.60$ ),<sup>52</sup> **thpy**-CN ( $517$  nm,  $\Phi = 0.60$ ) *vs.* **fac-Ir(thpy)<sub>3</sub>** ( $550$  nm,  $\Phi = 0.50$ ),<sup>53</sup> **piq**-CN ( $568$  nm,  $\Phi = 0.49$ ) *vs.* **fac-Ir(piq)<sub>3</sub>** ( $620$  nm,  $\Phi = 0.66$ ),<sup>53</sup> **TaBt**-CN ( $591$  nm,  $\Phi = 0.32$ ) *vs.* **Ir(TaBt)<sub>2</sub>(acac)** ( $650$  nm).<sup>54</sup>

The solid-state emission properties at RT and  $77$  K, in DMF/MeOH/EtOH ( $1 : 1 : 4$ , v/v/v) glassy solutions at  $77$  K (see Fig. S1–S5 in ESI†) and in  $2$  wt% doped PMMA thin films at RT were also examined (Table 1). Moreover, good accordance between the excitation spectrum and absorption spectrum of each iridium complex indicates that the emission arises from the complex purely. Absolute photoluminescence quantum yields (PLQYs)

were also measured for all the Ir(III) complexes. In  $\text{CH}_2\text{Cl}_2$  solutions, blue emitting Ir(III)-CN complexes ( $436$ – $454$  nm **dfppy**-CN, **dfppy**-CN, and **ppy**-CN) exhibit high PLQYs in the range of  $68$ – $84\%$ . It should be mentioned that the PLQY of **dfppy**-CN ( $80\%$ ) is one of the highest quantum yields ( $\Phi$ ) reported for deep-blue phosphors. Complexes **tmpi**-CN and **pmp**-CN display relatively lower PLQY ( $14\%$  and  $20\%$ ) in  $\text{CH}_2\text{Cl}_2$  solutions, while much higher PLQYs have been achieved in PMMA films (both are  $56\%$ ). And it is majorly attributed to the less perturbation on the triplet excited molecule from the surroundings in a rigid matrix (PMMA) than in solutions. The green and yellow phosphors (**thpy**-CN ( $517$  nm) and **lpt**-CN ( $545$  nm)) exhibit moderate PLQYs of  $60$ – $78\%$ . However, the PLQYs of orange and red phosphors are in a range of  $32$ – $49\%$  owing to the fast nonradiative decay rate at a long wavelength (energy gap law).<sup>55,56</sup> Compared with the counterpart Ir(III)-CN complexes, all Ir(III)-OCN and a few Ir(III)-Br complexes (**thpy**-Br and **piq**-Br) exhibit comparable PLQYs. Nevertheless, the Ir(III)-Br counterparts with blue emission show very low PLQYs ( $1.4\%$  for **dfppy**-Br and  $4\%$  for **ppy**-Br) and such behaviors are probably attributed to the instability of the Ir-Br bond for molecules in high triplet energy. Ultraviolet and deep-blue emitters **tmpi**-CN and **pmp**-CN with NHC moieties exhibit short emission lifetimes ( $1.73$  and  $0.87$   $\mu\text{s}$ ). The emission lifetimes of blue emitting Ir(III)-CN complexes are in the range of  $3.48$ – $7.39$   $\mu\text{s}$ . Furthermore, other Ir(III)-CN complexes with lower energy emission display much longer lifetimes ( $11.2$ – $36.65$   $\mu\text{s}$ ). It is worth noting that the emission lifetimes of these Ir(III) complexes bearing different monodentate ligands decrease in the order of Ir(III)-CN  $>$  Ir(III)-OCN  $>$  Ir(III)-Br.

## Electrochemistry studies

The electrochemical properties of selected Ir(III) complexes in degassed  $\text{CH}_2\text{Cl}_2$  have been assessed by cyclic voltammetry (CV) and the data are summarized in Table 2 (all values *versus* ferrocenium/ferrocene ( $\text{Fc}^{+/0}$ )). The cyclic voltammograms of these complexes in  $\text{CH}_2\text{Cl}_2$  are shown in Fig. 3 (Ir(III)-CN complexes) and Fig. S6† (Ir(III)-Br and Ir(III)-OCN complexes in ESI†). These complexes show one reversible oxidative wave in the range of  $0.43$ – $0.87$  V, except for **dfppy**-CN and **lpt**-CN which display one irreversible oxidative wave. The presence of electron-withdrawing substituents on the phenyl group leads to an anodic shift for the oxidation couple for **dfppy**-CN at  $0.72$  V to **ppy**-CN at  $0.59$  V (*vs.*  $\text{Fc}^{+/0}$ ). Furthermore, a more positive oxidation couple is observed for **dfppy**-CN ( $0.77$  V) than **dfppy**-CN ( $0.72$  V), which could be attributed to the electron-deficient properties of the pyridine group. The quasi-reversible/irreversible anodic waves of those complexes bearing **thpy**, **lpt**, **ppy** and **piq** ligands occur at  $\sim 0.6$  V *vs.*  $\text{Fc}^{+/0}$  showing a very slight difference in wave patterns. These trends are also observed in the group of Ir(III)-Br and Ir(III)-OCN complexes (Fig. S6 in ESI†). With the same bidentate ligands, the oxidation waves of Ir(III)-Br and Ir(III)-OCN complexes occur very closely, while that of Ir(III)-CN complexes occur around  $0.15$ – $0.19$  V greater (Table 2), implying that these anodic waves for these Ir(III) complexes come from the admixture of the phenyl part in



Table 2 Electrochemical<sup>a</sup> and thermogravimetry<sup>b</sup> data of Ir(III) complexes

Complex	$E_{\text{ox}}^{\text{c}}$ /V vs. $\text{Fc}^{+/0}$	$E_{\text{red}}^{\text{c}}$ /V vs. $\text{Fc}^{+/0}$	$E_g^{\text{d}}$ /eV	HOMO <sup>e</sup> /LUMO <sup>f</sup> /eV	$T_d^{98}$ /°C
tmpi-CN	(0.64)	—	3.75	−5.44/−1.69	350
pmp-CN	(0.67)	—	3.46	−5.47/−1.97	368
dfppy-CN	0.77	−2.53	3.07	−5.57/−2.50	355
dfppy-Br	0.55	(−2.57)	2.88	−5.35/−2.47	338
dfppy-CN	0.72	−2.66; (−2.59)	3.12	−5.52/−2.40	361
dfppy-OCN	0.57	(−2.61)	2.88	−5.37/−2.49	299
ppy-Br	0.43	(−2.68)	2.78	−5.23/−2.45	335
ppy-CN	0.59	−2.74; (−2.67)	2.97	−5.39/−2.42	372
ppy-OCN	0.44	(−2.67)	2.75	−5.23/−2.48	238
thpy-Br	0.42	(−2.63)	2.79	−5.32/−2.53	347
thpy-CN	0.61	(−2.69)	2.84	−5.41/−2.57	359
thpy-OCN	0.43	(−2.69)	2.79	−5.33/−2.54	306
piq-Br	0.44	−2.31	2.48	−5.24/−2.76	362
piq-CN	0.60	−2.29	2.69	−5.40/−2.71	376
piq-OCN	0.45	−2.29	2.48	−5.25/−2.77	343
lpt-CN	(0.56)	−2.40	2.66	−5.36/−2.70	250
TaBt-CN	0.69	−2.33	2.66	−5.49/−2.83	382

<sup>a</sup> Supporting electrolyte: 0.1 M  ${}^n\text{Bu}_4\text{NPF}_6$  in  $\text{CH}_2\text{Cl}_2$  and values are recorded vs. SCE;  $\text{Fc}^{+/0}$  occurs in the range of 0.48–0.51 V vs. SCE; scan rate: 100 mV s<sup>−1</sup>. <sup>b</sup> 2% weight loss in TGA measurements. <sup>c</sup> The values are reported versus  $\text{Fc}^{+/0}$ ; values without parentheses refer to  $E_{1/2}$  for reversible couples and with parentheses refer to the onset of the redox peak potential for the quasi/irreversible waves. <sup>d</sup>  $E_g = 1240/\lambda_{\text{onset}}(\text{UV})$ . <sup>e</sup> HOMO =  $−e(E_{\text{ox}} + 4.8)$ . <sup>f</sup> LUMO =  $E_g + \text{HOMO}$ .

$\text{C}^{\text{N}}$  ligands, the metal center and tridentate/monodentate ligands. With a strong  $\sigma$ -donating p orbital and a low-lying  $\pi$  orbital, the cyanide ligand strongly influences the metal centered frontier molecular orbital, thus leading to more positive  $E_{\text{ox}}$ .

On the other hand, these complexes display reduction waves ( $E_{\text{red}}$ ) in the range of −2.22 to −2.75 V vs.  $\text{Fc}^{+/0}$ , where those of the Ir(III)-CN complexes give reversible couples and those of the Ir(III)-Br or Ir(III)-OCN show irreversible waves. Impressively, the currents for the reversible reduction ( $i_{\text{e}}$ ) for the Ir(III)-CN complexes are almost equal to the currents for the oxidation ones (except  $i_{\text{e}}$  of reduction wave is nearly double to that of oxidation couples for **thpy-CN**), while these currents for the Ir(III)-Br and Ir(III)-OCN complexes are quite different (Fig. S7†). Particularly, for the piq group (**piq-Br**, **piq-OCN** and **piq-CN**), their reversible reduction couples occur at around −2.3 V vs.  $\text{Fc}^{+/0}$ , and the currents ( $i_{\text{e}}$ ) are equal to their oxidation couples. However, dfppy, ppy and thpy groups bearing Br and OCN as monodentate ligands display irreversible waves in the range of −2.57 to −2.69 V vs.  $\text{Fc}^{+/0}$ , and the currents of their reduction waves are several times the current intensities of their oxidation couples. In addition, complexes **lpt-CN** (−2.40 V), **piq-CN** (−2.29 V), **TaBt-CN** (−2.33 V) and **dfppy-CN** (−2.53 V) with greater  $\pi$ -conjugation ligands are capable of providing more positive reduction potentials with respect to **ppy-CN** (−2.74 V). All these imply that these reductions originated from the pyridinyl-ligand-based lowest unoccupied molecular orbital. And the cyanide monodentate ligand shows its advantage in electrochemical durability in this series of complexes in cyclic voltammetry studies.

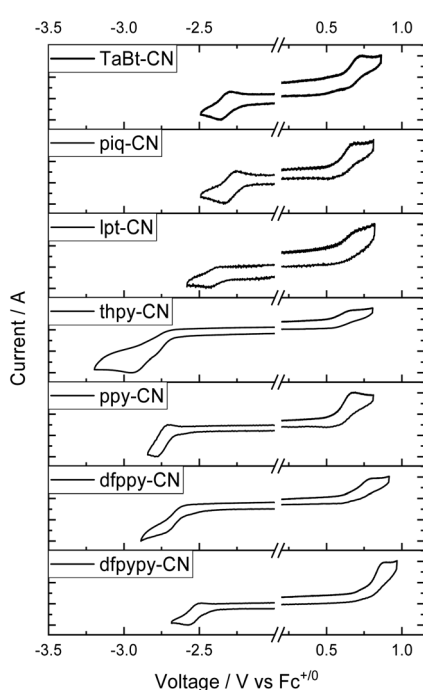


Fig. 3 Cyclic voltammograms of Ir(III)-CN complexes in  $-\text{CH}_2\text{Cl}_2$  with  ${}^n\text{Bu}_4\text{NPF}_6$  (0.1 M) as the supporting electrolyte. Conditions: scan rate: 100 mV s<sup>−1</sup>; glass-carbon, working electrode; Pt wire, counter electrode; saturated calomel electrode (SCE) in saturated KCl aqueous solution, and reference electrode.

### Thermal stability

Thermogravimetric analysis (TGA) and differential scanning calorimetry (DSC) experiments revealed the thermal stability of Ir(III) complexes (see Fig. S8 in ESI†). Most of the Ir(III)-CN complexes show good thermal stability (2 wt% loss > 350 °C, except for the decomposition temperatures ( $T_d$ ) of 250 °C for **lpt-CN**). TGA of the Ir(III)-Br complexes give  $T_d$  in the range of 335 to



362 °C which is 14–37 °C lower than that of Ir(III)–CN complexes. The Ir(III)–OCN complexes show the worst thermal stability in these groups, displaying  $T_d$  around 238–343 °C which is 28–134 °C lower than that of the Ir(III)–CN complexes. It is worth noting that, in the group of the same monodentate ligand, the trend of  $T_d$  increases with the formula weight of the Ir(III) complex. The reason for **Ipt-CN** showing the lowest  $T_d$  (250 °C) might be the steric effect in the back-forwarded iso-quinolinyl ligand in the **Ipt** ligand, resulting in a weak Ir–N bond. The glass transition temperatures ( $T_g$ ) of these complexes have not been observed prior to the decomposition of these complexes.

### Computational studies

To gain the insight into the electronic states, density functional theory (DFT) calculations (see the ESI† for details) have been performed to obtain the frontier molecular orbitals (MOs) of the selected complexes **dfppy-CN**, **dfppy-OCN**, **ppy-Br**, **ppy-CN**, **ppy-OCN**, **thpy-Br** and **Tabt-CN**. The geometry optimization in the calculations was employed using the crystal structure data, and the two highest occupied and lowest unoccupied molecular orbital (HOMO, HOMO–1, LUMO, and LUMO–1) surfaces and their corresponding energy levels are given in Fig. 4 and Table 3.

As shown in Fig. 4, the computed LUMOs are mainly located on the C≡N ligands for all these complexes; however the computed HOMOs are of mixed metal-ligand characteristics with the contributions from Ir 5d orbitals, phenyl units in C≡N ligands, the bis-NHC carbene pincer moiety and the monodentate ancillary. Ir 5d orbitals contribute over 35% in the HOMOs in most of these complexes, except for the **Tabt-CN** with 22.6%. Specifically, the participation of Ir 5d orbitals in the HOMO and HOMO–1 in the case of **dfppy-CN** is 38.6% and 40.2%, and their energy levels are quite close (−5.80 and −5.81 eV). The phenyl unit in C≡N ligands contribute differently in

Table 3 Calculated<sup>a</sup> MO energies and their % of metal contribution

Complex	H–2	H–1	HOMO	LUMO	L+1
<b>thpy-Br</b>	−6.07	−5.61	−5.42	−1.26	−0.74
		44.0%	37.8%	5.3%	2.0%
<b>Tabt-CN</b>	−6.14	−5.89	−5.58	−1.75	−0.50
		37.6%	22.6%	4.7%	2.4%
<b>dfppy-CN</b>	−6.32	−5.81	−5.80	−1.35	−0.80
		40.2%	38.6%	4.1%	2.5%
<b>dfppy-OCN</b>	−6.34	−5.83	−5.72	−1.40	−0.86
		40.6%	41.3%	3.9%	2.9%
<b>ppy-Br</b>	−6.03	−5.58	−5.49	−1.27	−0.79
		44.4%	44.25	3.5%	2.5%
<b>ppy-CN</b>	−6.22	−5.70	−5.67	−1.28	−0.83
		44.5%	45.5%	4.8%	3.7%
<b>ppy-OCN</b>	−6.23	−5.70	−5.60	−1.35	−0.89
		42.1%	42.6%	3.6%	3.0%

<sup>a</sup> PBE0/6-31G\* (LANL2DZ with ECP for Ir) level with PCM for modeling the  $\text{CH}_2\text{Cl}_2$  solvent.

these computed HOMOs. Owing to a large  $\pi$ -conjugation, the phenyl unit of **Tabt** contributes majorly in the HOMO of **Tabt-CN**. In turn, the phenyl unit of the bis-NHC pincer moiety was found to dominate the HOMO of the **dfppy-CN**, while the difluoro-phenyl unit of **dfppy** dominated its HOMO–1. The participation of both the bis-NHC carbene pincer moiety and monodentate ancillaries in the HOMOs of these complexes shows a reverse trend to the participation from the C≡N ligands. In the **ppy** group, cyanide show the lowest the HOMO energy levels compared to bromide and cyanate. And these observations are in consistent with the findings in the electrochemical studies.

Their computed UV-Vis profiles by time-dependent density functional theory (TDDFT) are summarized in Fig. S9 and Table S3 (ESI†). For the **ppy** group (−Br/−CN/−OCN), the three major

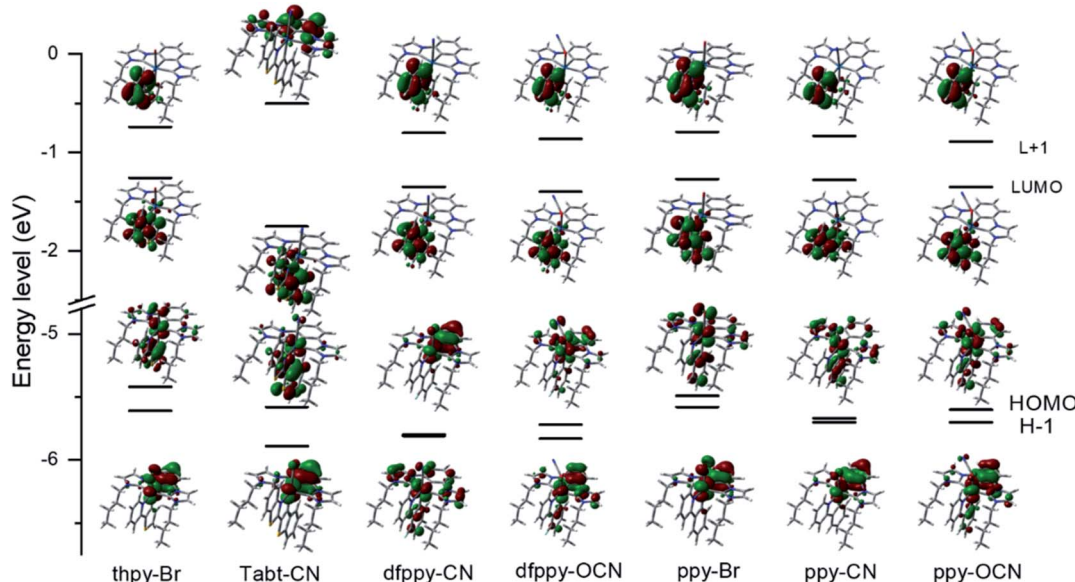


Fig. 4 (a) The computed frontier molecular orbitals energy levels and surfaces of **dfppy-CN**, **dfppy-OCN**, **ppy-Br**, **ppy-CN**, **ppy-OCN**, **thpy-Br**, and **Tabt-CN** at their ground state ( $S_0$ ) optimized geometry.



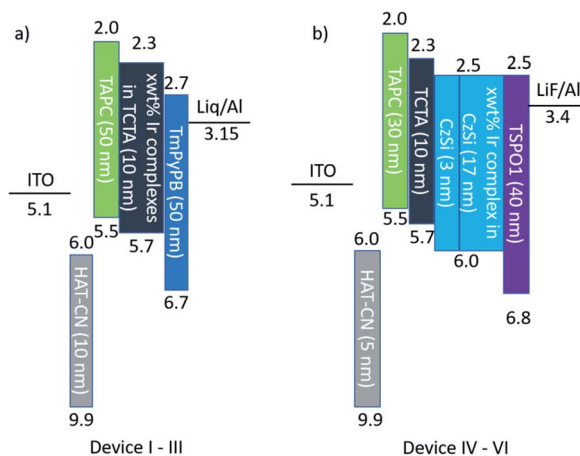


Fig. 5 Schematic energy-level diagram for the various layers used assuming vacuum level alignment.

absorption bands with  $\lambda > 250$  nm calculated are 290/269/290 nm, 320/310/327 nm, and 374/353/369 nm respectively, comparable to the bands from experiments (276/274/275 nm, 330/318/329 nm, and 372/356/372 nm). The lowest computed bands at 374/353/369 nm can be attributed to the transition of HOMO  $\rightarrow$  LUMO ( $>96\%$ ,  $S_1$ ) and the attribution for other bands

have been tabulated in Table S3 (ESI<sup>†</sup>). The lowest absorption bands for **dfppy-CN**, **dfppy-OCN**, **thpy-Br** and **TaBt-CN** were calculated to be 346 nm, 362 nm, 377 nm and 403 nm, giving the same trend as the observed 369 nm, 385 nm, 375 nm and 405 nm.

### Electroluminescence properties

To investigate the electroluminescence (EL) properties of **dfppy-OCN** (devices II and V), **ppy-OCN** (devices III and VI), and **dfppy-CN** (device V), multi-layer OLEDs, with schematic device configurations in Fig. 5, were fabricated by the thermal deposition technique (see the ESI<sup>†</sup> for details). For comparison, the OLEDs with **Flpic** (device I) were also fabricated as control devices. The EL characteristics of these devices are depicted in Fig. 6, Fig. S10 and S11.<sup>†</sup> Their key performances are listed in Table 3 (with a summary of some literature reported devices with  $CIE_y < 0.25$ ). As depicted in Fig. 6a, **dfppy-CN**, **dfppy-OCN** and **ppy-OCN** displayed EL spectra with the full width at half maxima (FWHMs) of around 60 nm at an optimized dopant concentration (Devices IV, V and VI).

With HOMO/LUMO levels at  $-5.7/-2.3$  eV and a  $E_T$  of 2.76 eV, 4,4',4''-tris(carbazol-9-yl)triphenylamine (TCTA) was used as a host material for **dfppy-OCN** (HOMO/LUMO levels of  $-5.37/-2.49$  eV and  $E_T$  of 2.78 eV), **ppy-OCN** ( $-5.23/-2.48$  eV

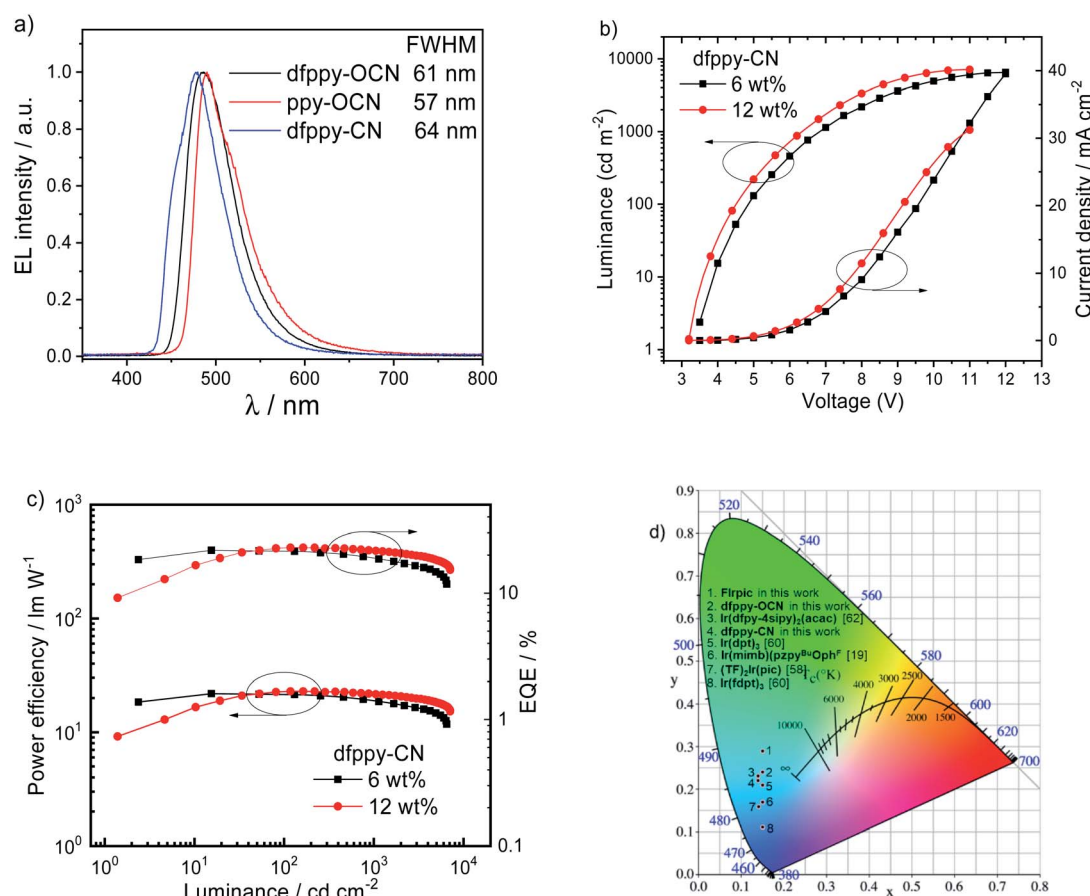


Fig. 6 (a) Normalized EL spectra of devices IV, V and VI, and (b)  $J-V-L$  characteristics and (c)  $\eta_{PE}-L - \eta_{Ext}$  characteristics of device IV with **dfppy-CN** at concentrations of 6 wt% and 12 wt%. (d) A CIE coordinates map of blue OLEDs with  $EQE_{max}$  over 15%.

Table 4 Key performance data for our OLED devices and some reported deep blue OLED devices with  $CIE_{x,y} < 0.25$ 

Dopants:Host/x wt% (Device)	EL	$V_{1/100/1000}^a$	$\eta_{L,max/100/1000}^b$	$\eta_{p,max/100/1000}^c$	$\eta_{Ext,max/100/1000}^d$	$CIE_{x,y}$	$L_{J_{1/2}/max}^e$	Ref.
<b>Irpic<sup>f</sup></b>								
TCTA/10 wt%	471	2.7/3.5/ 4.3	36.58/29.54/21.40 41.06/25.78/15.28	19.24/15.85/11.65	0.15, 0.29	6427/6680		
TCTA/20 wt% (I)	471	2.7/3.4/ 4.3	36.86/33.20/26.19 42.59/32.01/18.70	19.30/17.78/13.55	0.15, 0.31	9938/10 356		
TCTA/30 wt%	476	2.7/3.4/ 4.3	35.47/33.57/26.73 39.93/31.01/19.08	17.78/16.83/13.47	0.16, 0.33	11 955/12 804		
<b>dfppy-OCN<sup>f,g</sup></b>								
TCTA/10 wt%	471	3/3.9/5.4	15.75/13.77/7.92	15.53/10.82/4.44	8.26/7.63/4.78	0.15, 0.24	2531/2804	
TCTA/15 wt%	476	3/3.8/5	21.03/20.38/15.39	20.73/16.85/9.67	10.49/10.35/7.91	0.15, 0.27	4307/4749	
TCTA/20 wt% (II)	476	3/3.8/4.9	24.05/22.96/18.21	24.95/18.98/12.40	11.70/11.35/9.36	0.16, 0.29	5643/6240	
CzSi/18 wt%	485	3.2/4.4/ 6.4	41.40/38.94/34.58	37.91/27.18/16.73	18.83/17.87/16.16	0.16, 0.37	4027/6340	
CzSi/24 wt%	485	3/4.2/6.2	41.94/40.12/37.11	41.72/28.02/19.19	18.93/18.22/16.93	0.16, 0.38	4654/6800	
CzSi/30 wt% (V)	486	2.9/4/6	43.06/41.23/38.21	38.66/28.79/19.95	19.41/18.71/17.45	0.16, 0.39	5335/7100	
<b>ppy-OCN<sup>f,g</sup></b>								
TCTA/10 wt%	487	3/4.7/6.7	23.91/17.78/11.19	22.34/11.64/5.17	9.5/7.49/4.93	0.18, 0.38	5966/6722	
TCTA/20 wt% (III)	487	3/4.5/6.1	32.27/31.16/22.74	28.77/21.29/11.52	11.92/11.59/8.68	0.19, 0.46	10 032/11 383	
TCTA/30 wt%	488	3/4.7/6.3	32.28/31.89/25.18	29.55/20.89/12.36	11.67/11.58/9.31	0.20, 0.49	9375/11 262	
CzSi/4 wt% (VI)	488	3/4/5.4	45.72/44.00/33.74	38.07/34.56/17.45	16.67/16.05/12.28	0.19, 0.48	5219/6200	
CzSi/8 wt%	489	3/3.8/5.4	40.94/39.35/34.45	32.54/32.54/20.40	14.93/14.35/12.58	0.19, 0.49	5428/6790	
CzSi/12 wt%	490	3/3.8/5.2	39.21/38.40/36.54	35.00/31.75/20.08	14.72/14.42/13.72	0.20, 0.50	5478/6820	
<b>dfppy-CN<sup>g</sup></b>								
CzSi: 6 wt%	479	3/4.8/6.8	31.87/30.93/26.82	25.03/19.44/12.25	21.88/21.48/18.84	0.14, 0.22	4241/6500	
CzSi: 12 wt% (IV)	480	3/4.5/6.4	34.06/34.06/32.22	24.50/23.27/15.77	22.94/22.94/21.63	0.14, 0.24	4439/7100	
<b>Ir(fpmi)<sub>2</sub>(ppyz)</b>								
UGH2/4 wt%	466	4.2/—/—	11.8/—/—	7.4/—/—	9.1/—/—	0.14, 0.16	—/5668	44
UGH2-CzSi/4 wt%	470	4.3/—/—	19.7/—/—	13.8/—/—	14.1/—/—	0.14, 0.18	—/8161	
<b>Ir(fpmi)<sub>2</sub>(tfpyz)</b>								
UGH2-CzSi/4 wt%	454	4.9/—/—	6.5/—/—	4.1/—/—	7.6/—/—	0.14, 0.10	—/3446	44
<b>Ir(dfmbm)<sub>2</sub>(fptz)</b>								
UGH2/6 wt%	434, 460	4/—/—	6.3/3.0/—	4.0/0.9/—	6.0/2.7/—	0.158, 0.128	—/1000	38
<b>Ir(fbppz)<sub>2</sub>(dfbdp)</b>								
UGH2-CzSi/6 wt%	455	4.4/—/—	11.3/7.7/—	8.6/3.1/—	11.7/8.2/—	0.155, 0.106	—/4044	10
<b>Ir in mCPP01/10 wt%</b>								
(TF) <sub>2</sub> Ir(fptz)	448	3.3/ 4.5/—	8.6/7.53/—	8.1/5.25/—	8.4/7.36/—	0.174, 0.116	<1000/~1200	58
(TF) <sub>2</sub> Ir(pic)	460	3.3/ 4.4/—	21.7/21.31/—	19/15.20/—	17.1/16.83/—	0.141, 0.158	<2000/<2100	
(HF) <sub>2</sub> Ir(fptz)	448	3.4/ 4.8/—	9.1/7.78/—	7.7/5.09/—	8.4/7.1/—	0.149, 0.130	<300/~300	
(HF) <sub>2</sub> Ir(pic)	460	3.3/ 4.5/—	16.8/15.25/—	13.5/10.65/—	12.6/11.53/—	0.143, 0.169	~500/~500	
<b>mer-Ir(pmp)<sub>3</sub></b>								
TSPO1/20–8% graded	~435				14.4 ± 0.4/—/13.3 ± 0.1	0.16, 0.15	22 000 ± 1000/—	11
<b>fac-Ir(pmp)<sub>3</sub></b>								
TSPO1/20–8% graded	~460				10.1 ± 0.2/—/9.0 ± 0.1	0.16, 0.09	7800 ± 00/—	11
<b>Ir(dfpybpy)<sub>2</sub>(fpbpz)</b>								
SimCP: 20 wt%	440			4.14/—/—	7.0/—/—		<2000/<3000	59



Table 4 (Contd.)

Dopants:Host/x wt% (Device)	EL	$V_{1/100/1000}^a$	$\eta_{L,\max/100/1000}^b$	$\eta_{p,\max/100/1000}^c$	$\eta_{Ext,\max/100/1000}^d$	$CIE_{x,y}$	$I_{J_{1/2}/\max}^e$	Ref.
<b>Ir(mimb)(pzpy<sup>Bu</sup>Oph<sup>F</sup>)</b> DPEPO: 12 wt%	467	3.8/ 5.2/—	28.8/20.3/—	22.6/12.3/<5	20.7/14.6/<8	0.15, 0.17	<6000/<7000	19
<b>Ir(dfpy-4sipy)<sub>2</sub>(acac)</b> mCPPO1: 5 wt%		3.0/3.8/ 4.7	—/50.2/47.2	46.2/—/—	30.9/30.4/28.5	0.14, 0.24		62
<b>Ir(dfpy-4sipy)<sub>2</sub>(acac)</b> mCPPO1: 5 wt%		3.2/3.7/ 4.6	—/46.1/43.5	41.6/—/—	28.2/28.0/26.6	0.14, 0.23		
<b>Ir(fdpf)<sub>3</sub></b> DPEPO: 10 wt%		3.9/—/—	23.0/—/—	—/—/—	22.5/16.5/11.1	0.15, 0.11		60
DPEPO: 12 wt%		3.7/—/—	19.8/—/—	~15/—/—	19.4/17.8/12.6	0.15, 0.11	~3000/>3000	
<b>Ir(dp)<sub>3</sub></b> DPEPO: 12 wt%		3.5/—/—	36.0/—/—		21.9/21.2/21.0	0.15, 0.21	/20 070	

<sup>a</sup> Voltage at the luminance at 1/100/1000 cd m<sup>-2</sup>. <sup>b</sup> The maximum current efficiency ( $\eta_L$ ). <sup>c</sup> The maximum power efficiency ( $\eta_p$ ). <sup>d</sup> The maximum external quantum efficiencies ( $\eta_{Ext}$ ) and these values at 100 and 1000 cd m<sup>-2</sup>. <sup>e</sup> The value of luminance at half of its maximum current density ( $J_{1/2}$ ) and the maximum luminance. Device structures in this work:<sup>f</sup> and for Device (I), (II) or (III): ITO/HAT-CN (10 nm)/TAPC (50 nm)/TCTA (Ir complexes: x wt%, 10 nm; x = 10, 15, 20, 30)/TmPyPB (50 nm)/Liq (2 nm)/Al (120 nm),<sup>g</sup> and for Device (IV), (V) or (VI): ITO/HAT-CN (5 nm)/TAPC (30 nm)/TCTA (10 nm)/CzSi (3 nm)/CzSi (Ir complexes: x wt%, 17 nm; x = 4, 8, 12, 18, 24, 30)/TSPO1 (40 nm)/LiF (1.2 nm)/Al (100 nm).

and 2.70 eV), and **FIrpic** (−5.8/−2.9 eV (ref. 57) and 2.62 eV). The device structure was ITO/1,4,5,8,9,11-hexaazatriphenylenehexa-carbonitrile (HAT-CN, 10 nm)/1,1-bis[(di-4-tolylamino)phenyl]cyclohexane (TAPC, 50 nm)/TCTA:Ir complexes (10 nm)/1,3,5-tri(*m*-pyridin-3-ylphenyl)benzene (TmPyPB, 50 nm)/(8-hydroxyquino-linato)lithium (Liq, 2 nm)/Al (120 nm) (Fig. 5a) for Devices I–III. In these devices, TAPC and TmPyPB were used as hole-transporting-layer (HTL) and electron-transporting-layer (ETL) materials, respectively. The device performance was optimized by varying the concentration of Ir complexes, **dfppy-OCN**, **ppy-OCN**, or **FIrpic**, that were doped in TCTA as emitters in the emitting layer (EML). Maximum current efficiencies/power efficiencies ( $\eta_L/\eta_p$ ) of 24.1 cd A<sup>-1</sup>/25.0 lm W<sup>-1</sup> and 32.3 cd A<sup>-1</sup>/28.8 lm W<sup>-1</sup> were achieved at 20 wt% dopant concentration for **dfppy-OCN** (Device II) and **ppy-OCN** (Device III) while a maximum  $\eta_L/\eta_p$  of 36.9 cd A<sup>-1</sup>/41.4 lm W<sup>-1</sup> was achieved at 20 wt% for **FIrpic** (Device I). Maximum  $\eta_{Ext}$  values of 19.3, 11.9, and 11.7% were obtained for Devices I, II and III, respectively.

Since the  $E_T$  of 2.87 eV for **dfppy-OCN** was higher than that of TCTA (2.76 eV), **dfppy-OCN**-based OLEDs were fabricated with a configuration of ITO/HAT-CN (5 nm)/TAPC (30 nm)/TCTA (10 nm)/9-(4-*tert*-butylphenyl)-3,6-bis(triphenylsilyl)-9H-carbazole (CzSi, 3 nm)/CzSi: **dfppy-OCN** (17 nm)/diphenyl[4-(triphenylsilyl)-phenyl]phosphine oxide (TSPO1, 40 nm)/LiF (1.2 nm)/Al (100 nm). In these devices, CzSi (HOMO/LUMO level at −6.0/−2.5 eV)<sup>13</sup> and TSPO1 (HOMO/LUMO level at −6.8/−2.5 eV)<sup>61</sup> were used as host and ETL materials, respectively, because of their high  $E_T$  (3.02 eV (ref. 13) for CzSi and 3.36 eV (ref. 61) for TSPO1). An acceptable blue device with a maximum  $\eta_L/\eta_p/\eta_{Ext}$  of 34.1 cd A<sup>-1</sup>/24.5 lm W<sup>-1</sup>/22.9% was achieved with a dopant

concentration of 12 wt% for **dfppy-OCN** (Device IV). It is worth noting that the blue index, *i.e.*  $\eta_L/CIE_y$ , of 141.9 for Device IV at the luminance of 100 cd m<sup>-2</sup> is higher than those (typically lower than 120) of most reported Ir-based blue OLEDs with  $CIE_y$  below 0.25 except for the one using 5 wt% of **Ir(dfpy-4sipy)<sub>2</sub>(acac)**<sup>62</sup> in mCPPO1 whose blue index is 209.2 at 100 cd m<sup>-2</sup> (Table 4). Additionally, the  $\eta_{Ext}$  roll-off of 5.7% for Device IV at 1000 cd m<sup>-2</sup> is one of the best values among the blue OLEDs listed in Table 4. By adopting the same architecture, **dfppy-OCN** (Device V) and **ppy-OCN** (Device VI) show higher  $\eta_{Ext}$  and improved  $\eta_{Ext}$  roll-offs at 1000 cd m<sup>-2</sup>, attributable to the improved exciton confinement by the CzSi host and TSPO1 EML. Nonetheless, the color chromatic is still a challenge in our device performance; further device optimization and development of hosts with a suitable high triplet level for these blue emitting iridium complexes are still ongoing. Preliminary operational lifetime (LT) measurements for OLEDs with **ppy-OCN** and **ppy-OCN** were carried out under our laboratory conditions. The results are depicted in Fig. S12;† LT at 50% (LT<sub>50</sub>) of the initial luminance ( $L_0$ ) was 1.17 h at an  $L_0$  of 5000 cd m<sup>-2</sup> and 0.269 h at an  $L_0$  of 13 000 cd m<sup>-2</sup> for the **ppy-OCN**-based and **ppy-OCN**-based devices, respectively. For clear comparison, LT<sub>50</sub> values of 85.7 h for the **ppy-OCN**-based OLED and 99.9 h for the **ppy-OCN**-based one at  $L_0 = 400$  cd m<sup>-2</sup> were estimated by assuming the accelerate coefficient of 1.7.<sup>63</sup> In spite of similar LTs achieved in both devices, the maximum EQE (5.51%) of the **ppy-OCN**-based device used for LT measurements was much lower than that (13.3%) of the **ppy-OCN**-based one (see Fig. S12a†). Considering the high PLQY of 0.77 for **ppy-OCN** in the thin film (see Table 1), such a device structure might be



unsuitable for **ppy**-CN. By optimizing the device structure, longer LT is expected for **ppy**-CN-based OLEDs. It is worth noting that the LT<sub>50</sub> values for both **ppy**-CN-based and **ppy**-OCN-based devices are longer when compared with literature reported LT<sub>50</sub> (20.1 h) of devices with **FIrpic** at the same L<sub>0</sub>,<sup>64</sup> suggesting that the design strategy of [3 + 2 + 1] coordinated iridium complexes as phosphors in the application of OLEDs is effective.

## Conclusions

In conclusion, a series of neutral [3 + 2 + 1] iridium complexes bearing tridentate bis-NHC ligands, bidentate cyclometalated ligands and monodentate ligands has been successfully designed and synthesized. And these iridium complexes could display a wide range of phosphorescent emissions, which cover the UV and visible light range. The phosphorescent emission can be easily tuned by variation of the bidentate ligands. Among the three types of monodentate ligands in this study, the cyanide ion with strong  $\sigma$ -donor and weak  $\pi$ -acceptor properties shows abilities to (i) further increase the energy of the d-d states of the iridium atom and reduce the metal participation in the HOMO orbital and the excited states, thus leading to more ligand-centred transition characteristics in the absorption and longer emission lifetimes, (ii) stabilize the HOMO energy levels and the excited molecules in the high energy triplet state, (iii) slightly push the LUMOs up in blue and sky-blue emitters, (iv) increase the electrochemical durability in the cyclic voltammetry reduction process, and (v) improve the thermal stabilities. These iridium complexes show excellent absolute PLQYs with most them being over 50% and long emission lifetimes. And several blue and sky-blue emissive iridium complexes had been fabricated as devices. The device using **dfppy**-OCN as the sky-blue emitter at a dopant concentration of 20 wt% showed acceptable efficiencies compared to those of **FIrpic** in the same device structure but showed improved efficiency roll-offs at a high luminance of 1000 cd m<sup>-2</sup>. Particularly, a blue OLED (Device IV) with a blue index of 141.9 was achieved with **dfppy**-CN as the emitting dopant in the CzSi host with 12 wt% doping concentration at 100 cd m<sup>-2</sup>. The  $\eta_{\text{Ext}}$  roll-off of 5.7% for Device IV at 1000 cd m<sup>-2</sup> is one of the best values among blue OLEDs with Ir-emitters. The molecular-design strategy based on tridentate bis-NHC ligands and monodentate cyanide in the construction of [3 + 2 + 1] iridium complexes paves an alternative way for further development of phosphorescent plane displays.

## Data availability

(1) Crystallographic data for **thpy**-Br, **TaBt**-CN and **dfppy**-OCN have been deposited at the CCDC with CCDC No. of 2068837–2068839. (2) Date for this paper, including the photophysical, electrochemical, thermal properties, DFT calculation, device fabrication, synthesis of these complexes and their characterization are available in ESI, and can be downloaded from <https://doi.org/10.1039/d1sc01426a>.

## Author contributions

Y. W. and C. Y. wrote the manuscript, measured the crystallography, photophysical, electrochemical and thermal stability properties of these materials and analysed related data. J. L. contributed to the DFT calculations. Y. W., C. Y., M. Z., W.-S. L., and C.-C. W. synthesized these materials. W.-Q. L., G. C., and Q.-D. Y. fabricated and optimized the PhOLEDs. C. Y., G. C., Q.-D. Y. and G.-D. W. supervised the project, and analysed the data and they provided comments and revised the whole work with C.-M. C.

## Conflicts of interest

There are no conflicts to declare.

## Acknowledgements

W. Y., C. Y. and C.-C. Wu acknowledge Shenzhen PURI Materials Technologies, Co., Ltd. and colleague for their supports. This work was supported by the Guangdong Major Project of Basic and Applied Basic Research (2019B030302009), National Natural Science Foundation of China (NSFC No. 52003059), the Guangzhou Science and Technology Program (No. 202002030397), and the Shenzhen Science and Technology Innovation Committee (JCYJ20190809172615277 and JCYJ20200109150414471).

## Notes and references

- 1 C. Adachi, M. A. Baldo, M. E. Thompson and S. R. Forrest, *J. Appl. Phys.*, 2001, **90**, 5048–5051.
- 2 Y. Ma, H. Zhang, J. Shen and C.-M. Che, *Synth. Met.*, 1998, **94**, 245–248.
- 3 M. A. Baldo, D. F. O'Brien, Y. You, A. Shoustikov, S. Sibley, M. E. Thompson and S. R. Forrest, *Nature*, 1998, **395**, 151–154.
- 4 W. Song and J. Y. Lee, *Adv. Opt. Mater.*, 2017, **5**, 1600901.
- 5 S. E. Lee, T. V. Hoang, J.-H. Lee and Y. K. Kim, *Phys. B Condens. Matter*, 2018, **550**, 122–126.
- 6 M. H. Lu and J. C. Sturm, *Appl. Phys. Lett.*, 2001, **78**, 1927–1929.
- 7 N. Gupta, R. Grover, D. S. Mehta and K. Saxena, *J. Opt.*, 2015, **17**, 075402.
- 8 Y. Sun and S. R. Forrest, *Nat. Photonics*, 2008, **2**, 483–487.
- 9 C. Adachi, R. C. Kwong, P. Djurovich, V. Adamovich, M. A. Baldo, M. E. Thompson and S. R. Forrest, *Appl. Phys. Lett.*, 2001, **79**, 2082–2084.
- 10 Y.-C. Chiu, J.-Y. Hung, Y. Chi, C.-C. Chen, C.-H. Chang, C.-C. Wu, Y.-M. Cheng, Y.-C. Yu, G.-H. Lee and P.-T. Chou, *Adv. Mater.*, 2009, **21**, 2221–2225.
- 11 J. Lee, H.-F. Chen, T. Batagoda, C. Coburn, P. I. Djurovich, M. E. Thompson and S. R. Forrest, *Nat. Mater.*, 2016, **15**, 92–98.
- 12 H. Shin, Y. H. Ha, H.-G. Kim, R. Kim, S.-K. Kwon, Y.-H. Kim and J.-J. Kim, *Adv. Mater.*, 2019, **31**, 1808102.
- 13 E. Baranoff and B. F. E. Curchod, *Dalton Trans.*, 2015, **44**, 8318–8329.



14 S. Tokito, T. Iijima, Y. Suzuri, H. Kita, T. Tsuzuki and F. Sato, *Appl. Phys. Lett.*, 2003, **83**, 569.

15 R. J. Holmes, S. R. Forrest, Y. J. Tung, R. C. Kwong, J. J. Brown, S. Garon and M. E. Thompson, *Appl. Phys. Lett.*, 2003, **82**, 2422–2424.

16 M. A. Baldo, S. Lamansky, P. E. Burrows, M. E. Thompson and S. R. Forrest, *Appl. Phys. Lett.*, 1999, **75**, 4–6.

17 M. A. Baldo, M. E. Thompson and S. R. Forrest, *Nature*, 2000, **403**, 750–753.

18 Y.-J. Su, H.-L. Huang, C.-L. Li, C.-H. Chien, Y.-T. Tao, P.-T. Chou, S. Datta and R.-S. Liu, *Adv. Mater.*, 2003, **15**, 884–888.

19 H. H. Kuo, Y. T. Chen, L. R. Devereux, C. C. Wu, M. A. Fox, C. Y. Kuei, Y. Chi and G. H. Lee, *Adv. Mater.*, 2017, **29**, 1702464.

20 P. Gnanasekaran, Y. Yuan, C. S. Lee, X. Zhou, A. K. Jen and Y. Chi, *Inorg. Chem.*, 2019, **58**, 10944–10954.

21 C.-Y. Kuei, S.-H. Liu, P.-T. Chou, G.-H. Lee and Y. Chi, *Dalton Trans.*, 2016, **45**, 15364–15373.

22 H. H. Kuo, Z. L. Zhu, C. S. Lee, Y. K. Chen, S. H. Liu, P. T. Chou, A. K. Jen and Y. Chi, *Adv. Sci.*, 2018, **5**, 1800846.

23 L.-Y. Hsu, Q. Liang, Z. Wang, H.-H. Kuo, W.-S. Tai, S.-J. Su, X. Zhou, Y. Yuan and Y. Chi, *Chem.-Eur. J.*, 2019, **25**, 15375–15386.

24 A. J. Wilkinson, H. Puschmann, J. A. K. Howard, C. E. Foster and J. A. G. Williams, *Inorg. Chem.*, 2006, **45**, 8685–8699.

25 P. Brulatti, R. J. Gildea, J. A. K. Howard, V. Fattori, M. Cocchi and J. A. G. Williams, *Inorg. Chem.*, 2012, **51**, 3813–3826.

26 Y. Koga, M. Kamo, Y. Yamada, T. Matsumoto and K. Matsubara, *Eur. J. Inorg. Chem.*, 2011, **2011**, 2869–2878.

27 K. C. Chan, W. K. Chu, S. M. Yiu and C. C. Ko, *Dalton Trans.*, 2015, **44**, 15135–15144.

28 S. Obara, M. Itabashi, F. Okuda, S. Tamaki, Y. Tanabe, Y. Ishii, K. Nozaki and M.-a. Haga, *Inorg. Chem.*, 2006, **45**, 8907–8921.

29 L. Fu, M. Pan, Y.-H. Li, H.-B. Wu, H.-P. Wang, C. Yan, K. Li, S.-C. Wei, Z. Wang and C.-Y. Su, *J. Mater. Chem.*, 2012, **22**, 22496.

30 L. Yang, F. Okuda, K. Kobayashi, K. Nozaki, Y. Tanabe, Y. Ishii and M.-a. Haga, *Inorg. Chem.*, 2008, **47**, 7154–7165.

31 J. Kuwabara, T. Namekawa, E. Sakabe, M.-a. Haga and T. Kanbara, *J. Organomet. Chem.*, 2017, **845**, 189–195.

32 T. Fleetham, G. Li and J. Li, *Adv. Mater.*, 2017, **29**, 1601861.

33 J. Brooks, Y. Babayan, S. Lamansky, P. I. Djurovich, I. Tsypa, R. Bau and M. E. Thompson, *Inorg. Chem.*, 2002, **41**, 3055–3066.

34 L. Flamigni, A. Barbieri, C. Sabatini, B. Ventura and F. Barigelli, Photochemistry and Photophysics of Coordination Compounds: Iridium, in *Photochemistry and Photophysics of Coordination Compounds II. Topics in Current Chemistry*, ed. V. Balzani and S. Campagna, Springer Berlin/Heidelberg, 2007, vol. 281, pp. 143–203.

35 D. Jacquemin and D. Escudero, *Chem. Sci.*, 2017, **8**, 7844–7850.

36 A. F. Rausch, L. Murphy, J. A. G. Williams and H. Yersin, *Inorg. Chem.*, 2012, **51**, 312–319.

37 T. Sajoto, P. I. Djurovich, A. Tamayo, M. Yousufuddin, R. Bau, M. E. Thompson, R. J. Holmes and S. R. Forrest, *Inorg. Chem.*, 2005, **44**, 7992–8003.

38 C. F. Chang, Y. M. Cheng, Y. Chi, Y. C. Chiu, C. C. Lin, G. H. Lee, P. T. Chou, C. C. Chen, C. H. Chang and C. C. Wu, *Angew. Chem., Int. Ed.*, 2008, **47**, 4542–4545.

39 K. Li, G. Cheng, C. Ma, X. Guan, W.-M. Kwok, Y. Chen, W. Lu and C.-M. Che, *Chem. Sci.*, 2013, **4**, 2630–2644.

40 R. Visbal and M. C. Gimeno, *Chem. Soc. Rev.*, 2014, **43**, 3551–3574.

41 C. Yang, F. Mehmood, T. L. Lam, S. L.-F. Chan, Y. Wu, C.-S. Yeung, X. Guan, K. Li, C. Y.-S. Chung, C.-Y. Zhou, T. Zou and C.-M. Che, *Chem. Sci.*, 2016, **7**, 3123–3136.

42 P. Pinter, J. Soellner and T. Strassner, *Chem.*, 2019, **25**, 14495–14499.

43 M. N. Hopkinson, C. Richter, M. Schedler and F. Glorius, *Nature*, 2014, **510**, 485–496.

44 C. H. Hsieh, F. I. Wu, C. H. Fan, M. J. Huang, K. Y. Lu, P. Y. Chou, Y. H. Yang, S. H. Wu, I. C. Chen, S. H. Chou, K. T. Wong and C. H. Cheng, *Chem.-Eur. J.*, 2011, **17**, 9180–9187.

45 L.-H. Chung, H.-S. Lo, S.-W. Ng, D.-L. Ma, C.-H. Leung and C.-Y. Wong, *Sci. Rep.*, 2015, **5**, 15394.

46 T. P. Hanusa, Cyanide Complexes of the Transition Metals, in *Encyclopedia of Inorganic Chemistry*, ed. D. J. Burkey, 1st edn, 2005, pp. 1–11, DOI: DOI: 10.1002/0470862106.ia059.

47 K. Dedeian, J. Shi, E. Forsythe, D. C. Morton and P. Y. Zavalij, *Inorg. Chem.*, 2007, **46**, 1603–1611.

48 R. D. Sanner, N. J. Cherepy and V. G. Young, *Inorganica Chim. Acta*, 2016, **440**, 165–171.

49 A. K. Pal, S. Krotkus, M. Fontani, C. F. R. Mackenzie, D. B. Cordes, A. M. Z. Slawin, I. D. W. Samuel and E. Zysman-Colman, *Adv. Mater.*, 2018, **30**, e1804231.

50 S. J. Lee, K.-M. Park, K. Yang and Y. Kang, *Inorg. Chem.*, 2009, **48**, 1030–1037.

51 A. B. Tamayo, B. D. Alleyne, P. I. Djurovich, S. Lamansky, I. Tsypa, N. N. Ho, R. Bau and M. E. Thompson, *J. Am. Chem. Soc.*, 2003, **125**, 7377–7387.

52 A. F. Rausch, M. E. Thompson and H. Yersin, *Inorg. Chem.*, 2009, **48**, 1928–1937.

53 S. Okada, H. Iwawaki, M. Furugori, J. Kamatani, S. Igawa, T. Moriyama, S. Miura, A. Tsuboyama, T. Takiguchi and H. Mizutani, *SID Symp. Dig. Tech. Pap.*, 2002, **33**, 1360–1363.

54 Mitsubishi Chemical Corp., Japan, *JP. Pat.*, 4192592, 2008.

55 J. V. Caspar and T. J. Meyer, *J. Phys. Chem.*, 1983, **87**, 952–957.

56 J. V. Caspar, E. M. Kober, B. P. Sullivan and T. J. Meyer, *J. Am. Chem. Soc.*, 1982, **104**, 630–632.

57 V. I. Adamovich, S. R. Cordero, P. I. Djurovich, A. Tamayo, M. E. Thompson, B. W. D'Andrade and S. R. Forrest, *Org. Electron.*, 2003, **4**, 77–87.

58 S. Lee, S. O. Kim, H. Shin, H. J. Yun, K. Yang, S. K. Kwon, J. J. Kim and Y. H. Kim, *J. Am. Chem. Soc.*, 2013, **135**, 14321–14328.

59 C.-H. Yang, M. Mauro, F. Polo, S. Watanabe, I. Muenster, R. Fröhlich and L. De Cola, *Chem. Mater.*, 2012, **24**, 3684–3695.

60 X. Li, J. Zhang, Z. Zhao, L. Wang, H. Yang, Q. Chang, N. Jiang, Z. Liu, Z. Bian, W. Liu, Z. Lu and C. Huang, *Adv. Mater.*, 2018, **30**, e1705005.

61 S. O. Jeon, S. E. Jang, H. S. Son and J. Y. Lee, *Adv. Mater.*, 2011, **23**, 1436–1441.



62 R. Zaen, K.-M. Park, K. H. Lee, J. Y. Lee and Y. Kang, *Adv. Opt. Mater.*, 2019, **7**, 1901387.

63 C. Féry, B. Racine, D. Vaufrey, H. Doyeux and S. Cinà, *Appl. Phys. Lett.*, 2005, **87**, 213502.

64 S. Yi, J.-H. Kim, Y.-J. Cho, J. Lee, T.-S. Choi, D. W. Cho, C. Pac, W.-S. Han, H.-J. Son and S. O. Kang, *Inorg. Chem.*, 2016, **55**, 3324–3331.

